POLITECNICO DI TORINO
Repository ISTITUZIONALE

Sustainable Synthesis of PDoped Carbon Nitride From Fertilizer Sources for Enhanced Photocatalysis

Original
Sustainable Synthesis of PDoped Carbon Nitride From Fertilizer Sources for Enhanced Photocatalysis / Cartabia, Luca; Dubinina, Yana; Barbieri, Marianna; Wlazo, Mateusz; Schweitzer, Pascal; Wang, Mengjiao; Lamberti, Francesco; Zoppellaro, Giorgio; Schlettwein, Derck; Smarsly, Bernd; Osella, Silvio; orevi, Luka; Giusto, Paolo; Gatti, Teresa. - In: CHEMPHOTOCHEM. - ISSN 2367-0932. - 10:5(2026), pp. 1-13. [10.1002/cptc.202600008]

Availability:
This version is available at: 11583/3010547 since: 2026-05-05T08:26:49Z

Publisher:
John Wiley and Sons

Published
DOI:10.1002/cptc.202600008

Terms of use:

This article is made available under terms and conditions as specified in the corresponding bibliographic description in the repository

Publisher copyright

(Article begins on next page)

31 May 2026

Check for updates

ChemPhotoChem

Chemistry Europe
European Chemical Societies Publishing
ChemPhotoChem

RESEARCH ARTICLE OPEN ACCESS

Sustainable Synthesis of P-Doped Carbon Nitride From Fertilizer Sources for Enhanced Photocatalysis

Luca Cartabia[1,2] | Yana Dubinina[1,2] | Marianna Barbieri[3] | Mateusz Wlazło[4] | Pascal Schweitzer[1,5] | Mengjiao Wang[6] | Francesco Lamberti[3] | Giorgio Zoppellaro[7] | Derck Schlettwein[1,5] | Bernd Smarsly[1,2] | Silvio Osella[4] | Luka Đorđević[3] | Paolo Giusto[8] | Teresa Gatti[1,2,6]

[1]Center for Materials Research, Justus Liebig University, Giessen, Germany | [2]Institute of Physical Chemistry, Justus Liebig University, Giessen, Germany | [3]Department of Chemical Sciences, University of Padova, Padova, Italy | [4]Materials and Processes Simulation Lab, Centre of New Technologies, University of Warsaw, Warszawa, Poland | [5]Institute of Applied Physics, Justus Liebig University, Giessen, Germany | [6]Department of Applied Science and Technology, Politecnico di Torino, Torino, Italy | [7]Regional Centre of Advanced Technologies and Materials, Faculty of Science, Palacký University Olomouc, Olomouc, Czech Republic | [8]Department of Colloid Chemistry, Max Planck Institute of Colloids and Interfaces, Potsdam, Germany

Correspondence: Paolo Giusto (paolo.giusto@mpikg.mpg.de) | Teresa Gatti (teresa.gatti@polito.it)

Received: 7 January 2026 | **Revised:** 23 March 2026 | **Accepted:** 17 April 2026

Keywords: carbon nitride | environmental remediation | phosphorus doping | photocatalysis | sustainable synthesis

ABSTRACT

The contamination of rivers, lakes, and oceans by synthetic toxic dyes has become a critical issue that is undermining water safety around the globe. Metal-free semiconductors, and in particular the family of carbon nitrides, represent an appealing solution to degrade pollutants triggered by solar light illumination. Here, we present a new fabrication strategy for phosphorus-doped carbon nitride starting from two abundant fertilizers widely used in agriculture: thiourea and diammonium phosphate. We show that in the resulting P-doped carbon nitride P is incorporated by substitution of C atoms in the lattice, eventually increasing the population of photoexcited states and efficiently suppressing charge-carrier recombination. Doped samples, and specifically the one obtained with an initial 1 %wt of P dopant in the precursor, demonstrate superior abilities in the degradation of four persistent dyes (Rhodamine B, malachite green, indigo carmine, Congo red) compared to the pristine carbon nitride. This P-doped semiconductor efficiently catalyzes the quantitative photodegradation of common dyes in less than 60 min, thus proving noteworthy versatility and applicability for use in environmental remediation applications.

1 | Introduction

The rapid industrialization mankind experienced in the last two centuries has fostered human progress and the advancement of science, leading to the expansion of knowledge and wealth. Nevertheless, all of this came with severe environmental costs in terms of air, soil, and water pollution, which the new generations of scientists are called to face [1]. In particular, the scarcity and contamination of water sources are regarded as one of the greatest challenges of our times [2, 3].

Synthetic organic dyes account for an estimated 17%–20% of industrial wastewater pollution, posing a severe threat to aquatic ecosystems and human health [4]. Their high molar absorptivity reduces light penetration in water, depriving aquatic organisms of necessary solar radiation, while their chemical stability renders many conventional wastewater treatment methods ineffective [5]. Photocatalysis has emerged as a promising strategy to remove and mineralize these pollutants. Using only light and an appropriate semiconductor catalyst, pollutants can be oxidized into harmless end products such as CO_2 and H_2O. When the semiconductor absorbs light, electron–hole pairs are generated and can participate in interfacial redox reactions. This leads to the formation of reactive oxygen species (ROS), including hydroxyl ($HO^{\bullet}$) and superoxide

This is an open access article under the terms of the Creative Commons Attribution License, which permits use, distribution and reproduction in any medium, provided the original work is properly cited.

© 2026 The Author(s). *ChemPhotoChem* published by Wiley-VCH GmbH.

($O_2^{\bullet-}$) radicals, which effectively degrade the organic dye molecules in solution.

Among several semiconductors, carbon nitrides have gained a pivotal role as suitable photocatalysts for a broad spectrum of processes, including water splitting [6], CO_2 reduction [7], and environmental remediation [8]. In recent years, carbon nitrides have also attracted considerable attention for biomedical research, hence expanding their applicability even beyond the field of catalysis [9, 10]. The interest in this class of semiconductors arises from their nontoxicity, cheap and facile fabrication, medium bandgap (2.7 eV) enabling the absorption in the visible range, and great thermal and chemical stability [11, 12]. The term "carbon nitrides" actually refers to a broader family of compounds that includes different polymorphs (α-C_3N_4, β-C_3N_4), C/N ratios (C_3N_4, C_3N_5), and ionic structures (poly (heptazine imides), poly(triazine imides)) [13–15]. Each class of carbon nitrides has unique properties that arise from their composition, spatial configuration, and electronic properties. This enables a wide range of applicability in a variety of fields, including fabrication of hard materials [16], solar energy storage and conversion [17], electrocatalysis [18], photocatalysis [19–21], and photoelectrocatalysis [22]. Among the broad scope of carbon nitride materials, heptazine-based carbon nitride, whose ideal parent structure is the "graphitic carbon nitride" (g-C_3N_4), encompasses the presence of residual hydrogen ($C_xN_yH_z$) from nonideal condensation and short-range order in the structure [23]. For this reason, the term "polymeric carbon nitride" [24] has been introduced to describe g-C_3N_4 with incomplete condensation, and hereafter referred to simply as "CN".

Regarding the synthetic methodology, CN is usually obtained by thermal condensation of suitable N-rich organic precursors such as melamine, urea, thiourea, cyanamide, and dicyanamide, at temperatures between 500°C and 600°C [25–28]. The synthetic procedure and the choice of precursors greatly influence the physico-chemical properties of the final material. Different precursors undergo decomposition and condensation at varying rates, which strongly affect the degree of polymerization and the structural order in the final CN. Melamine condenses rapidly, typically yielding denser structures with higher crystallinity, whereas urea and thiourea condense more slowly, leading to more porous and less polymerized materials. The lower degree of polymerization of these CN materials introduces more structural defects that can be beneficial for photocatalysis [29–31].

CN typically suffers from poor electrical conductivity, restricted absorption interval, low specific surface area (SSA), and fast charge recombination [32, 33]. Therefore, exploiting its structural tunability, researchers have focused on doping CN with heteroatoms to overcome its intrinsic limitations and enhance the photocatalytic activity. Nonmetal elements such as O [34], S [35], B [36], and halogens [37–39] have stemmed as dopants for CN since they allow improved photocatalytic performances, via tuning of the band edges and suppression of charge recombination, without the need for precious or critical metals. Recently, doping with phosphorus has attracted increasing attention since P atoms can be incorporated into the carbon nitride backbone, boosting the photocatalytic activity toward various processes like H_2 evolution [40], H_2O_2 production [41], N_2 reduction [42], and degradation of pollutants [43]. However, the use of P-doped CN is still in its infancy, and the underlying catalytic mechanisms of action of this emerging material are still not fully understood.

In this work, we address the existing gap in synthetic approaches and the mechanistic understanding of the photodegradation process. We report a straightforward synthesis of P-doped CN derived from thiourea and diammonium phosphate, two widely available fertilizers [44, 45]. A thorough physico-chemical characterization reveals successful inclusion of phosphorus by replacement of C atoms in the CN lattice, leading to great suppression of exciton recombination. The final material tested in photocatalytic processes provides superior performance and high versatility in the degradation of four different water-polluting dyes. By simple centrifugation, the P-doped semiconductor can be easily recovered and reused while retaining its catalytic efficiency. The mechanistic pathways are investigated by a combination of scavenger experiments, EPR studies, and H_2O_2 colorimetric assays to unravel the production of ROS and their role in the photocatalytic reactions. The oxidation of benzylic substrates in acetonitrile is also employed as a further study to probe the activity of P-doped CN in a different solvent and reaction environment.

2 | Results and Discussion

The synthesis of P-doped CN is straightforward. Thiourea (T) is used as the precursor of CN, while diammonium phosphate (AP; $(NH_4)_2HPO_4$) is the source of P (Figure 1). The two reagents are first dissolved in deionized H_2O to achieve an optimal mixing,

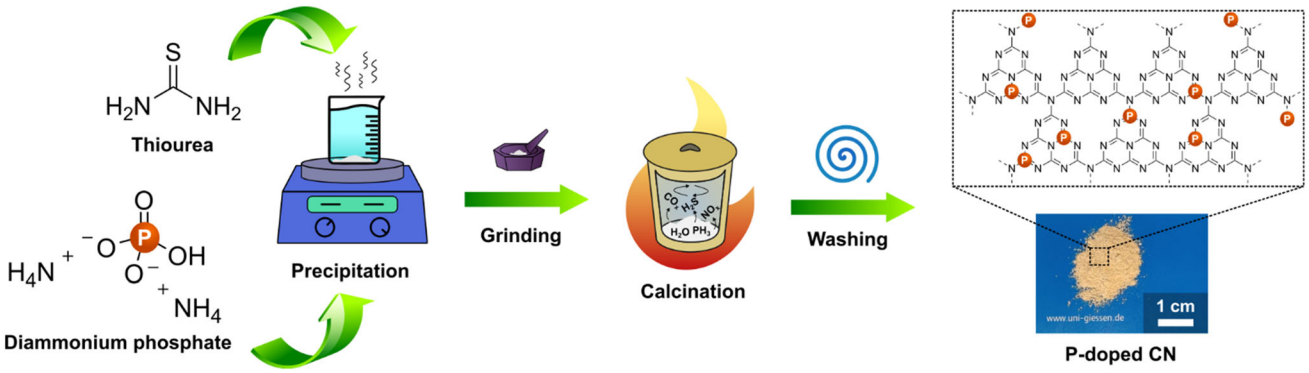

FIGURE 1 | Schematic illustration of the synthesis of P-doped CN starting from thiourea as CN precursor and diammonium phosphate as phosphorus source. Upon calcination of the precipitate at 550°C, thermal polymerization occurs, and orange powders are obtained.

23670932, 2026, 5, Downloaded from https://chemistry-europe.onlinelibrary.wiley.com/doi/10.1002/cptc.202600008 by Politecnico Di Torino Sist. Bibl Del Polit Di Torino, Wiley Online Library on [14/05/2026]. See the Terms and Conditions (https://onlinelibrary.wiley.com/terms-and-conditions) on Wiley Online Library for rules of use; OA articles are governed by the applicable Creative Commons License

and upon evaporation of the solvent, the precipitate is collected and calcined at 550°C. By varying the amount of diammonium phosphate (AP), we prepared samples with increasing phosphorus content (wt%): TAP_0.5 (0.5 wt% P), T-AP_1 (1.0%wt P), T-AP_1.5 (1.5 wt% P), and T-AP_2 (2.0 wt% P).

Scanning electron microscopy (SEM) micrographs (Figure 2) show the evolution of morphology from a denser and layered-like structure typical of 2D materials (T-CN Figure 2a) to a more amorphous one with the formation of large cavities upon doping with 1 wt% (T-AP_1, Figure 2d) and 2 wt% of phosphorous (T-AP_2, Figure 2g). These cavities are attributed to the release of volatile species during thermal condensation. This morphological transformation of the materials was also investigated with N_2 physisorption, which shows a small SSA that increases significantly (three to more than fourfold) upon P-doping (Figure S1a in the Supporting Information). All the samples display type II isotherms with H3 hysteresis loops, according to the IUPAC classification, corresponding to typical mesoporous materials featuring open slit-shaped pores and a disordered porous network [46, 47]. The calculation of the pore size distributions also confirmed an increasing mesoporous character of the specimen, whose pore network evolves with P-doping (Figure S1b in the Supporting Information). Such a disordered system of pores and cavities of variable dimensions is most likely due to the outburst of endogenous gases generated from the condensation and decomposition of the precursors. In the pristine T-CN, the structure is denser and the pore size distribution features lower mesoporous content since the only volatile species generated are due to the condensation of thiourea. When AP is added, the volume of endogenous gases increases. These act as porogens thus

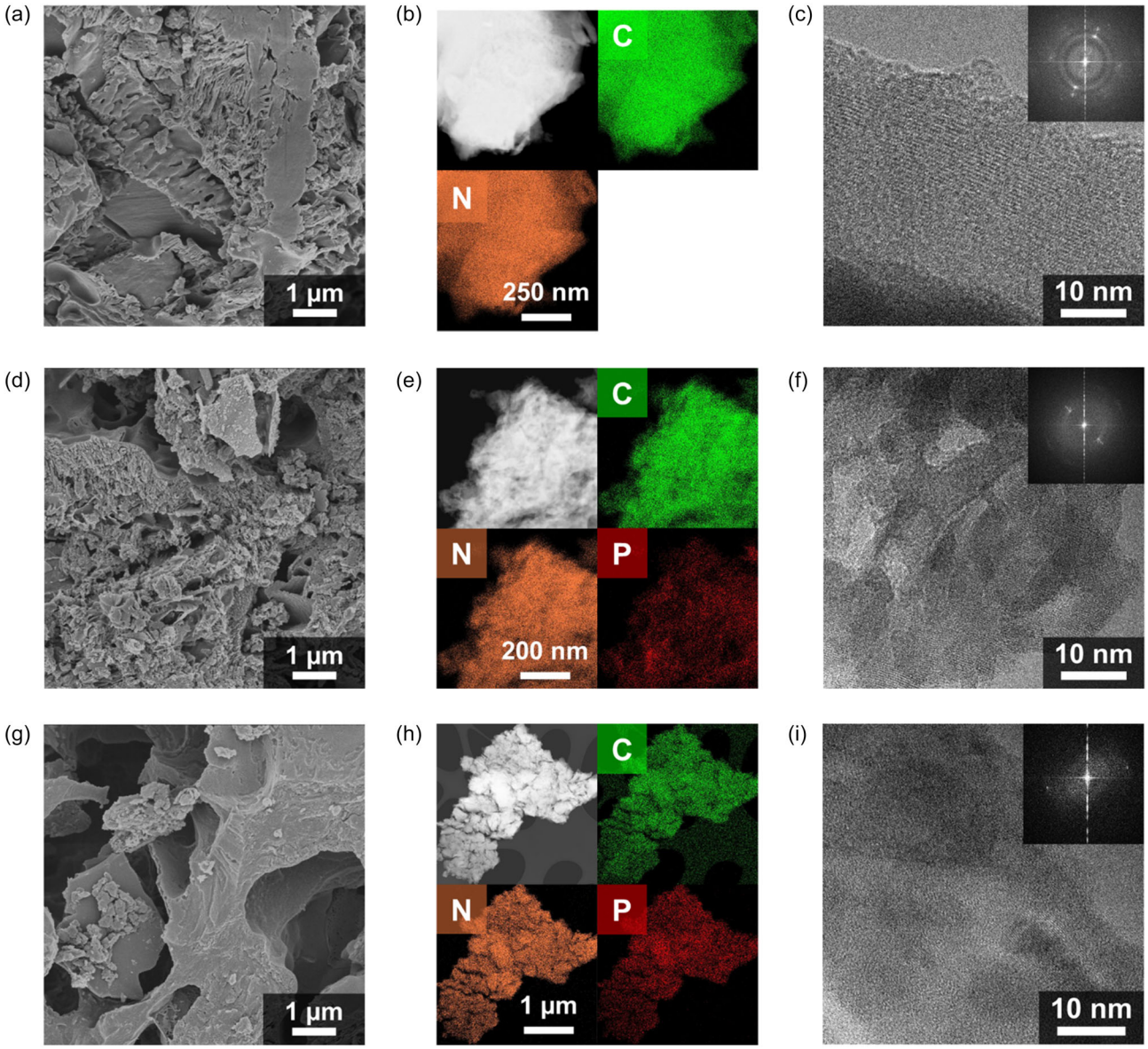

FIGURE 2 | SEM micrographs (left column; a,d,g), EDX elemental mappings (central column; b,e,h), and TEM images with SAED insets (right column; c,f,i) of T-CN (photos a–c), T-AP_1 (photos d–f), and T-AP_2 (photos g–i). The formation of a porous network is clearly visible going from pristine CN (a) to T-AP_1 (d) and T-AP_2 (g). Uniform P doping is confirmed by EDX for both T-AP_1 (e) and T-AP_2 (h), compared to T-CN (b). The ordered crystalline domains found in TEM and SAED of the undoped CN (c) evolve into smaller crystallites in T-AP_1 (f) and become even fewer and more distorted in T-AP_2 (i).

23670932, 2026, 5, Downloaded from https://chemistry-europe.onlinelibrary.wiley.com/doi/10.1002/cptc.202600008 by Politecnico Di Torino Sist. Bibl Del Polit Di Torino, Wiley Online Library on [14/05/2026]. See the Terms and Conditions (https://onlinelibrary.wiley.com/terms-and-conditions) on Wiley Online Library for rules of use; OA articles are governed by the applicable Creative Commons License

leading to samples with a more pronounced mesoporous character in the pore size distribution and improved SSA (T-AP_0.5 and T-AP_1). The higher AP content in T-AP_1.5 and T-AP_2 determines an even larger volume of endogenous gases. During the calcination, they escape from the powders, leaving behind a network of larger pores visible at SEM (see the evolution of pore size from T-AP_1 in Figure 2d to T-AP_2 in Figure 2g), resulting in a more random pore size distribution and a slightly lower SSA (Figure S1a,b).

The morphological studies were integrated with compositional analysis performed with energy-dispersive X-ray spectroscopy (EDX). The obtained maps show a uniform distribution of phosphorus in T-AP_1 (Figure 2e) and T-AP_2 (Figure 2h) samples, pointing to a homogeneous doping with P without preferential aggregation. As expected, the P signal is totally absent in the pristine T-CN (Figure 2b). The increasing amount of AP in the precursor mixture is successfully reflected in an increased percentage of P in the final P-doped CN, ranging from 0.64 % at (T-AP_0.5) to 3.6 %at (T-AP_2) (see Table S1 in the Supporting Information).It must be noted that little to no sulfur (≤0.1%at) was measured by EDX in pristine and P-doped CN samples.

At the nanoscale, transition electron microscopy (TEM) shows the structure and symmetry of the samples, thanks also to the selected area electron diffraction (SAED) technique. Pristine CN shows ordered crystalline domains with a slightly distorted hexagonal pattern (Figure 2c), probably due to the sulfur impurities induced by the use of thiourea. The inclusion of P, which has a larger atomic radius than C and N, introduces higher disorder in the lattice, as shown by the T-AP_1 (Figure 2f) and T-AP_2 (Figure 2i) images, in good agreement with X-ray diffraction (XRD) patterns (Figure 3a). The latter display the characteristic (100) and (002) reflections of CN materials, which account for the in-plane order and the interlayer stacking along the crystallographic *c* axis, respectively [48]. The (100) signal is found at a 2θ value of 13.0° for all samples, whereas the (002) position decreases in value with increasing P doping, as clearly visible by zooming in this area. The shift from 27.4° in the pristine sample (T-CN) to 27.1° (T-AP_2) is due to the incorporation of the relatively large P atoms in the lattice, which causes an expansion of the (00*l*) interlayer distance [41]. Alongside the change in position, the full-width-at-half-maximum significantly increases, and the intensity of the (002) reflection decreases. This indicates that P-doped CNs are characterized by shorter-range order than the undoped ones.

Fourier transform infrared (FT-IR) spectroscopy was used to further probe the structure of the obtained materials. The corresponding spectra exhibit broad absorption in the 3400–3000 cm^{-1} range typical of uncondensed amino groups and $-NH_2$ terminal moieties, and O–H bonds of adsorbed water (Figure 3b). The bands in the region from 1700 to 1200 cm^{-1} are ascribed to the characteristic combination of C=N stretching modes of the CN heterocycles [49]. The breathing of the heptazine ring is also observed at 805 cm^{-1} [50]. All the samples show the typical spectroscopic features of CN materials constituted by heptazine units, thus correlating with previous characterization. Upon doping, a slight broadening of the peak at 888 cm^{-1} is also noticeable, which can indicate a structural change in the material induced by the incorporation of phosphorus. The vibrations of the P–N bonds do not clearly emerge in the spectral region from 1200 to 900 cm^{-1} due to the overlapping strong absorption arising from the CN heterocycles [51].

Surface chemical properties are critical for catalytic performances, and thereby X-ray photoelectron spectroscopy (XPS) provides pivotal information. Survey spectra were first measured scanning all over the instrumental range of binding energies, finding the characteristic peaks of P 2*s* and P 2*p* electrons in the series from T-AP_0.5 to T-AP_2 (Figure S2b in the Supporting Information). The relative chemical composition of P in all samples is higher than the one measured by EDX (Table S1 in the Supporting Information), pointing to a surface enrichment in P. High-resolution spectra were measured for C 1*s*, N 1*s*, O 1*s*, and P 2*p* electrons to evaluate the chemical bonds (Figure 4). The C 1*s* signal of all the samples can be fitted with 4 components: the main arise from electrons involved in the –N–C=N– (288.2 to 288.4 eV), C–C (284.8 eV), and C–NH_x (286.2 to 286.4 eV) bonds, while the peak at 289.4 eV is ascribed to C–O bonds formed as defects during the calcination in air [52]. The deconvolution of the N 1*s* region shows the characteristic signals of carbon nitride for electrons of –C–N=C– (398.7 to 398.5 eV), N–$(C)_3$ (399.6 to 399.8 eV), and H–N–C (400.9 to 401.1 eV) bonds. However, in the doped samples, a shoulder at lower values of binding energy indicates the presence of N–P bonds (397.3 eV), which grows in intensity and area with increasing

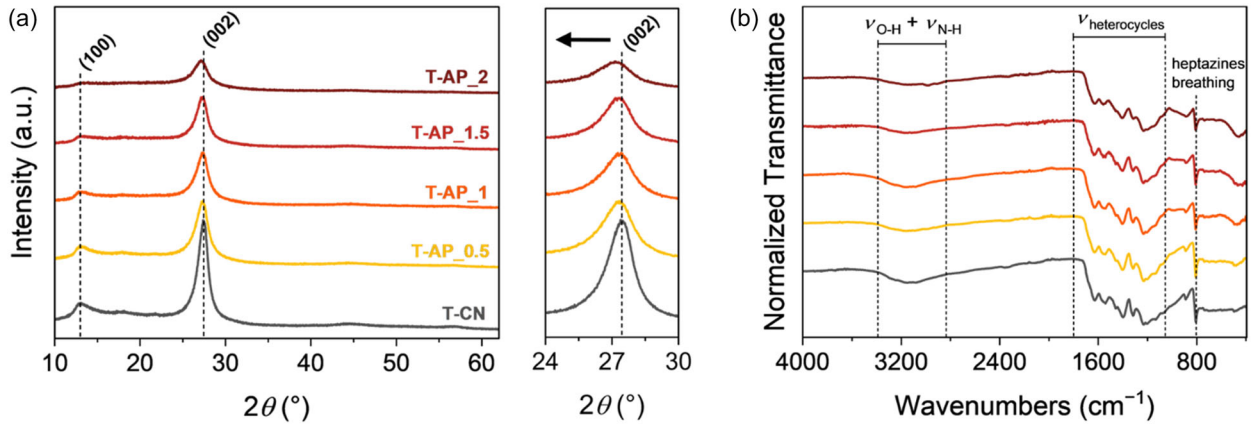

FIGURE 3 | XRD patterns of all the CN samples with a detail of the shifting of (002) reflection upon P-doping marked by the arrow (a), and FT-IR spectra with highlighted regions for CN characteristic bands (b).

23670932, 2026, 5, Downloaded from https://chemistry-europe.onlinelibrary.wiley.com/doi/10.1002/cptc.202600008 by Politecnico Di Torino Sist. Bibl Del Polit Di Torino, Wiley Online Library on [14/05/2026]. See the Terms and Conditions (https://onlinelibrary.wiley.com/terms-and-conditions) on Wiley Online Library for rules of use; OA articles are governed by the applicable Creative Commons License

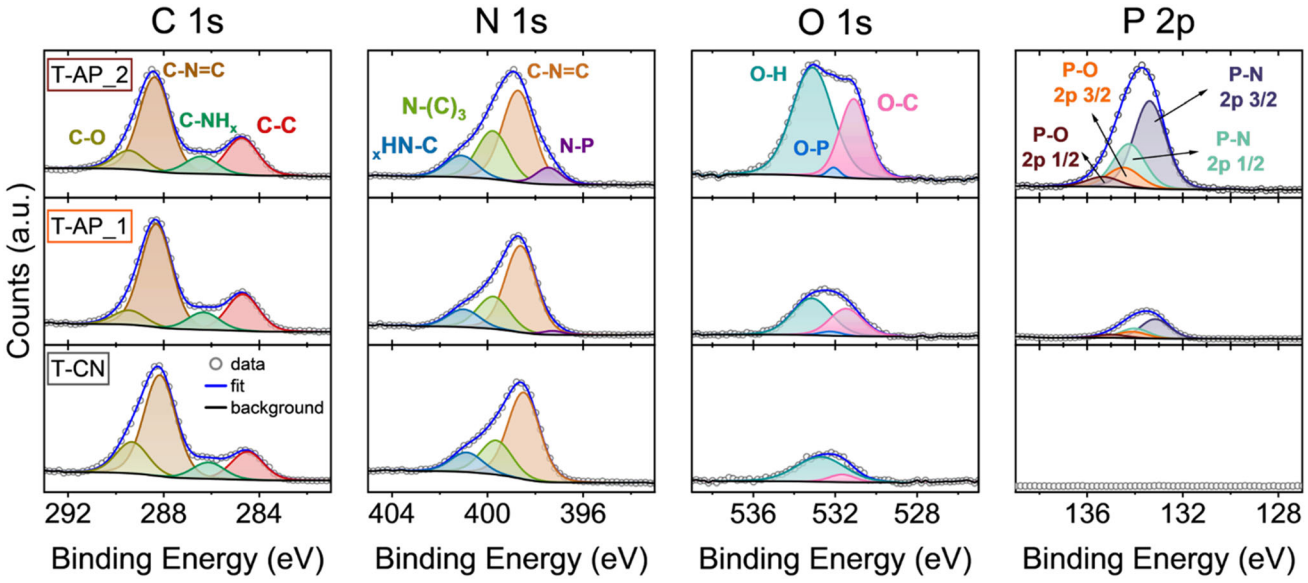

FIGURE 4 | XPS high-resolution spectra of sample T-CN (bottom-row graphs), T-AP_1 (middle-row graphs), and T-AP_2 (top-row graphs) in the regions of C 1*s*, N 1*s*, O 1*s*, and P 2*p* orbitals (from left to right). The experimental data is represented by empty gray dots, the blue line is the fitting, and the black line is the Shirley's background function. All the spectra share the same *y*-axis dimension. In the N 1*s* region, the component of electrons involved in N–P bonds (highlighted in violet) is clearly emerging upon doping, thus showing the substitution of C atoms by P. The O–P and P–O peaks of residual phosphates are visible in the O 1*s* and P 2*p* regions, respectively.

P content [53]. A similar trend is found in O 1*s* spectra, where the O–P signal of residual phosphates from diammonium phosphate is rising at 532.1 eV upon doping [54]. This causes a broadening of the overall signal compared to the T-CN one, thus shifting the O–H component of residual adsorbed water and the O–C peak to slightly higher (533.1 eV) and slightly lower (531.1 eV) binding energies, respectively. The P 2*p* region is characterized by a major contribution from P–N electrons of 2*p* 3/2 (133.3 eV) and 2*p* 1/2 (134.2 eV) orbitals with a splitting of 0.9 eV, which indicates the presence of P atoms in the P-doped CN backbone. A minor contribution from P–O electrons of 2*p* 3/2 (134.5 eV) and 2*p* 1/2 (135.4 eV) orbitals featuring the same splitting accounts for residual phosphates, hence matching the O–P peak found in O 1*s* spectra [55]. The region of S 2*p* orbitals was also probed (Figure S2c in the Supporting Information), but it features little to no signal emerging from the background, hence correlating with the extremely scarce sulfur content detected with EDX. Generally, XPS indicates that P is introduced in the CN structure by replacing the C of the heptazine units, which also explains the trend in decreasing C/N and increasing P/C ratios found with elemental analysis and EDX, respectively (Table S1 in the Supporting Information). All these structural and electronic signatures consistently confirm that P substitutes C within the heptazine framework while simultaneously contributing to the observed increase in SSA.

The spectroscopic characterizations of the materials are of paramount importance for their application in photocatalysis, as they provide information on the electronic properties, absorption edge, recombination, and the presence of unpaired electrons. Diffuse reflectance UV–vis spectroscopy (DRS UV–vis) can be used to establish the absorption edge and to calculate the bandgap of the synthesized materials. From the spectra in Figure 5a, all the samples show a steep absorption edge at 450 nm, with no significant differences, and characteristic absorbance in the UV range. The tail in the green >480 nm is a typical feature of thiourea-derived CN, and it is due to synthesis-induced structural defects, vacancies, or impurities [25, 56]. No specific absorption related to phosphorus doping is noticeable in the spectra. This agrees with experimental observations since the color of the as-prepared powders showed no significant difference, regardless of the dopant precursor concentration (Figure S2a in the Supporting Information).

The optical bandgap (E_{gap}) values reported assuming a direct semiconductor behavior show negligible variation from 2.79 eV for the undoped CN to 2.84 eV for T-AP_1 (Figure 5b and Table S2 in the Supporting Information) [57]. However, the energies of the valence band maximum (E_{VB}), conduction band minimum (E_{CB}), and Fermi level (E_F) are expected to change upon doping. Therefore, valence-band XPS (Figure S2d in the Supporting Information) and Kelvin probe force microscopy (KPFM; Figure S3 in the Supporting Information) were used to calculate the difference between the Fermi level and the valence band (E_F–E_{VB}) and the work function (Φ) of the prepared semiconductors, respectively (Table S2 in the Supporting Information). The combination of these techniques and the E_{gap} values calculated from DRS UV–V is allowed us to reconstruct the energy levels of the materials (Figure 5c). Although doping does not seem to affect the bandgap, the inclusion of P perturbates the electronic system of the material, causing a clear shift of the band levels toward more negative energy (vs. vacuum), or in other words, making P-doped CN significantly more oxidative.

With this regard, models of pristine and P-doped heptazine-based gC_3N_4 structures were constructed with varying doping schemes that mimic T-CN, TAP_1, and TAP_2 samples. Structural and electronic parameters of these model systems were computed using periodic density functional theory (DFT) calculations at the PBE-D3(BJ) level of theory. Specifically, P doping was

23670932, 2026, 5, Downloaded from https://chemistry-europe.onlinelibrary.wiley.com/doi/10.1002/cptc.202600008 by Politecnico Di Torino Sist. Bibl Del Polit Di Torino, Wiley Online Library on [14/05/2026]. See the Terms and Conditions (https://onlinelibrary.wiley.com/terms-and-conditions) on Wiley Online Library for rules of use; OA articles are governed by the applicable Creative Commons License

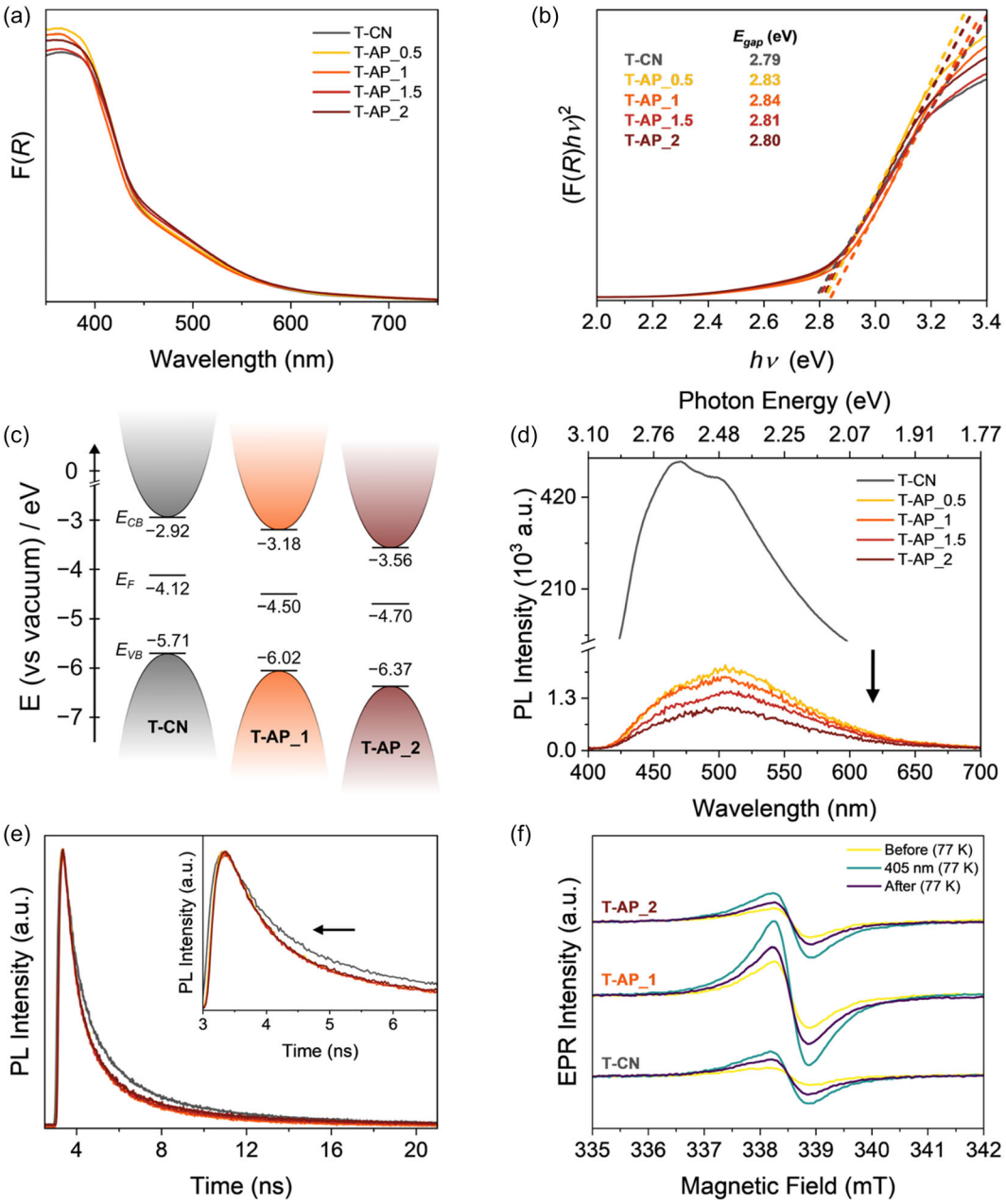

FIGURE 5 | DRS UV–vis spectra of pristine and P-doped CN samples (a). Tauc plots calculated assuming a direct semiconductor behavior, and the corresponding bandgap energy values (E_{gap}) showing no substantial difference with each other (b). Band structure scheme of pristine and P-doped CN calculated by the combination of DRS UV–vis, KPFM, and valence-band XPS data (c). SS-PL spectra recorded in water solution after excitation at 400 nm; the arrow highlights a strong quenching of the measured PL due to efficient suppression of radiative charge recombination upon doping (d). TCSPC spectra showing PL decay in time (e); the inset reports a magnification of the main signal, which highlights faster recombination (i.e., shorter lifetime of charge carriers) than the pristine sample, as indicated by the arrow. CW-EPR spectra of selected solid samples measured at 77 K prior (yellow), during (green), and after 10 min illumination (violet) with a 405 nm LED (f).

introduced in the form of C atom substitution, either at C1 (corner of heptazine unit) or C2 (edge of heptazine unit) sites, and distributed uniformly in the material to emulate a bulk doping. With the supercell approach, introducing 5 and 8 P atoms leads to a doping of 2.23% and 3.57%, closely resembling the T-AP_1 and T-AP_2 samples, respectively (Tables S3 and S4 in the Supporting Information). After optimization of the lattice and atomic degrees of freedom, we observe that doping leads to lattice expansion in every direction. The higher the doping, the more the lattice is expanded to accommodate the increased size of P atoms, which substitute carbon (Table S4 in the Supporting Information). We noticed a considerable difference depending on whether C1 or C2 sites are substituted. The lattice expands more in the case of C1 substitution, both in the stacking plane and in the out-of-plane direction. Energetically, the C2 substitution is most stable in both T-AP_1 and T-AP_2 by −23 and −46 meV, respectively, compared to the C1-substituted bulk. Additionally, a mixed C2/C1 substitution was considered, and it resulted in the lowest energy stability (i.e., less table structure compared to the C2 substitution) by 134 meV. When P substitutes

23670932, 2026, 5, Downloaded from https://chemistry-europe.onlinelibrary.wiley.com/doi/10.1002/cptc.202600008 by Politecnico Di Torino Sist. Bibl Del Polit Di Torino, Wiley Online Library on [14/05/2026]. See the Terms and Conditions (https://onlinelibrary.wiley.com/terms-and-conditions) on Wiley Online Library for rules of use; OA articles are governed by the applicable Creative Commons License

C, an additional electron per doping site is introduced into the unit cell. This leads to a shift of the Fermi level, which now resides above the CB, and as a result, the Kohn–Sham gap (VB to CB eigenvalue difference) decreases. However, the difference between VB and the lowest unoccupied CB (the first one above the Fermi level) is slightly higher than the Kohn–Sham gap in pristine CN (Table S4 in the Supporting Information). This may explain the apparent widening of the experimental optical bandgap. The VB of undoped and doped CN consists entirely of N(p) orbitals (Figures S4 and S5 in the Supporting Information), while the CB of pristine CN consists of mixed C(p) and N(p) orbitals, dominated by C(p), as evidenced by atom-projected density of states (PDOS). When P is introduced, all the bands are shifted down in energy, and now the Fermi level crosses the CB. While the VB still consists of N(p) orbitals, the CB shows a mix of the three atoms, in which the P contribution depends on its position and amount. Overall, these observations are in line with the experimental band character, thus confirming the crucial role of P for band edges modulation.

The optical properties of the newly synthesized P-doped CN materials were further studied by steady-state photoluminescence (SS-PL) and transient photoluminescence spectroscopies (TR-PL) and compared to those of pristine CN. SS-PL spectra of the doped samples show a considerable PL compared to the pristine one upon excitation at 400 nm (Figure 5d), and a redshift of the maxima position. The drop in signal intensity follows the increasing phosphorus content, meaning that P-doping successfully suppresses radiative charge recombination of the CN semiconductor [58]. TR-PL carried out by time-correlated single photon counting (TCSPC) allows to investigate the charge carriers' lifetime, revealing a slightly shorter lifetime in all the doped materials with respect to T-CN (Figure 5e). In particular, the signals can be well fitted with a tri-exponential decay in which the contribution of the component τ_1, which accounts for emission in the shortest time scale, grows with the P atomic percentage (Figure S6 and Table S5 in the Supporting Information). Combining the SS-PL and the TR-PL data, it is clear that the inclusion of phosphorous strongly hinders the recombination of the photogenerated electrons and holes, which is only possible with lower radiative intensity and in a shorter time frame compared to the undoped T-CN, thus showing good chances for increased efficiency of charge transfer for photocatalytic redox processes.

Continuous-wave electron paramagnetic resonance spectroscopy (CW-EPR) was further performed to compare the radical defects of undoped and P-doped CN under dark and illuminated conditions (Figure 5e). In pristine T-CN, the conduction band (CB) is largely C 2p′(π^*) in character, whereas the valence band (VB) is dominated by N 2p (lone-pair) states. Upon photoexcitation, electron (e^-)/hole (h^+) pairs form; the electrons preferentially localize in C-rich π^* states and produce a nearly isotropic resonance at $g = 2.003$, characteristic of carbon-centered spins. Weak hyperfine coupling of these CB electrons to nearby ^{14}N nuclei ($I = 1$) manifests as slight broadening rather than resolved hyperfine lines. In contrast, holes tend to localize on N-rich motifs and experience stronger, anisotropic ^{14}N hyperfine and quadrupolar interactions, which shorten spin–spin relaxation time T_2 and broaden the hole signal beyond detection in CW-EPR. Moreover, heterogeneity in both undoped and P-doped samples further increases inhomogeneous linewidths, obscuring any individual ^{14}N or ^{31}P ($I = 1/2$) splitting. Across all samples, the CW-EPR spectra collected during dark-light cycles show a single, approximately Gaussian line, the intensity of which increases under illumination. The magnitude of this light-induced intensity gain depends on phosphorus doping: P incorporation does not markedly alter the g-value or the line shape but increases the number of free charge carriers (probed by CW-EPR), which are central in photocatalysis as they can promote specific chemical reactions [59]. With this regard, T-AP_1 stems from its highest charge separation as well as lowest recombination efficiency, which should be a strong support for the enhanced photocatalytic process.

Morphological and spectroscopical characterizations suggest that the P-doped materials possess improved specific surface and outstanding charge separation properties, thus holding great promise for the photodegradation of polluting dyes. Therefore, the photocatalytic activity of all the samples was tested in the degradation of four common water-polluting toxic dyes widely employed in industry: Rhodamine B (RhB), malachite green (MG), indigo carmine (IC), and Congo red (CR) [5]. These molecules have very different structures and functional groups, which is ideal to test the activity of a photocatalyst on a broader range of chemically different compounds. The experiments were conducted in a 50 μM water solution of the dyes under the illumination of a blue LED with a sharp emission at 400 nm (Figure 6), and the extent of the degradation was evaluated via UV–vis spectroscopy. All the detailed procedures, parameters, and setups used for these tests are available in the Supporting Information. Figure 6a shows the performance of the samples in the degradation of MG. A neat increase in the degradation efficiency characterizes the P-doped samples, which outperforms T-CN. In particular, a full decolorization is reached within 50 min with T-AP_1, whereas at a higher percentage of phosphorus, the process is slower. Similarly, testing the other dyes (Figure S8b–d in the Supporting Information), T-AP_1.5 and T-AP_2 demonstrate an even worse activity than T-CN, while T-AP_1 shows the best performance. The rate constants were calculated assuming first-order kinetics of dye degradation, and the resulting values are reported in Figure S9 in the Supporting Information. Across the different dye molecules tested, similar volcano plots were obtained, with T-AP_1 emerging as the most active catalyst, thus allowing the fastest reactions. For MG degradation, in particular, a first-order rate constant $k = 0.10287\ \mathrm{cm}^{-1}$ was calculated for T-AP_1, thus showing noteworthy performances when compared to other CNs [60], MOFs [61], and biochar nanocomposites [62] recently reported in literature. This correlates well with the increased population of photoexcited states found in the CW-EPR spectra of T-AP_1. In this context, dopant concentration is a critical parameter that significantly alters the electronic structure of the catalyst, possibly resulting in less favorable excitonic splitting when the doping percentage exceeds the optimal one. Recyclability experiments also demonstrate that T-AP_1 is able to retain its photocatalytic activity over consecutive reaction cycles with MG (Figure 6b) and similarly with all the other dyes (Figure S10a–c in the Supporting Information). Investigations on the role of T-AP_1 in MG degradation were carried out by adding selected scavenger species to the initial reaction mixture. The results are reported in Figure 6c, which also shows the starting pH measured after the addition of the scavenger in large excess. Indeed, scavengers often carry acidic or basic

23670932, 2026, 5, Downloaded from https://chemistry-europe.onlinelibrary.wiley.com/doi/10.1002/cptc.202600008 by Politecnico Di Torino Sist. Bibl Del Polit Di Torino, Wiley Online Library on [14/05/2026]. See the Terms and Conditions (https://onlinelibrary.wiley.com/terms-and-conditions) on Wiley Online Library for rules of use; OA articles are governed by the applicable Creative Commons License

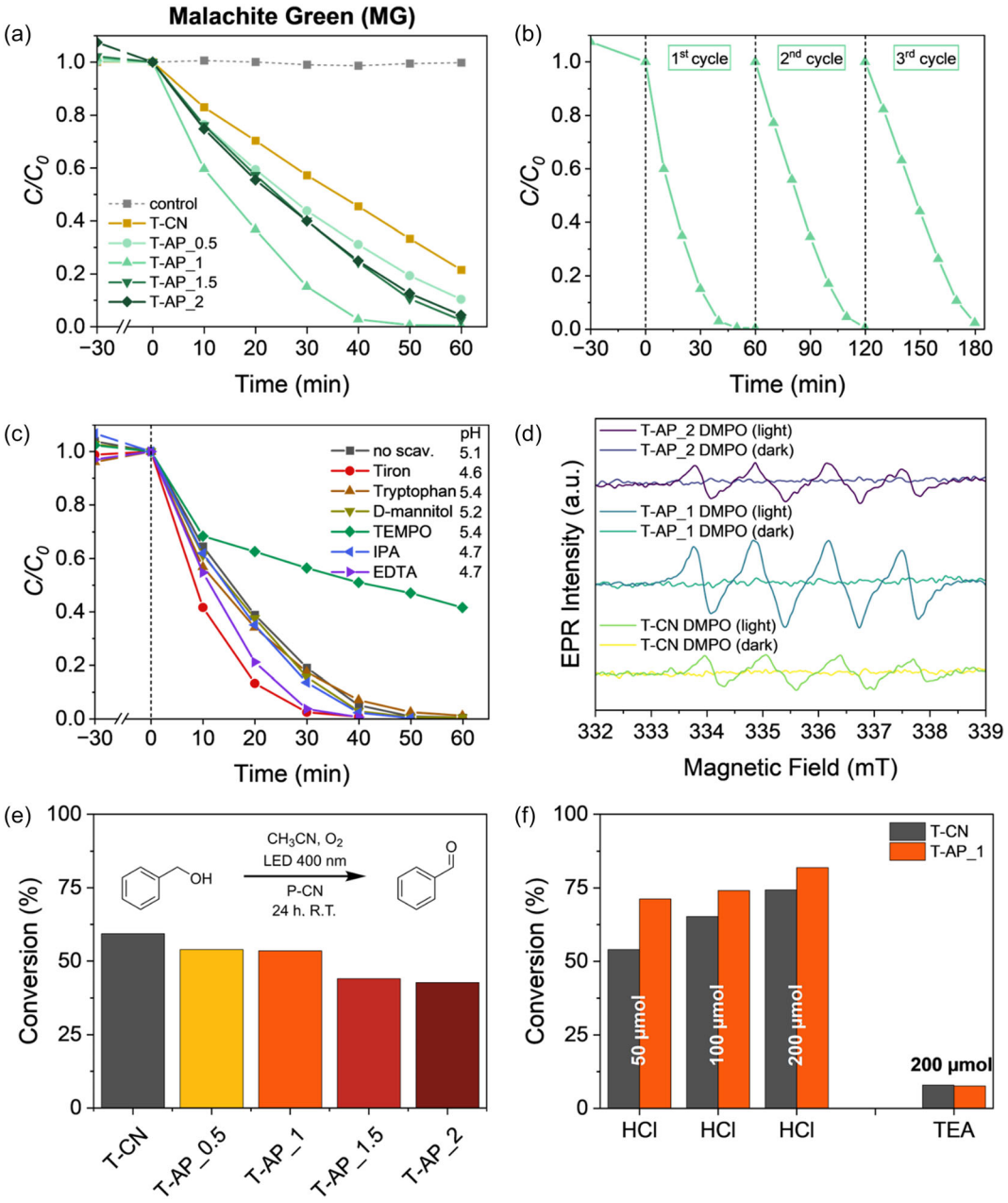

FIGURE 6 | Photocatalytic degradation of MG using pristine T-CN, P-doped samples, and a "control" with no catalyst (a). Recyclability experiments of T-AP_1 in 3 consecutive catalytic runs of MG degradation (b). Scavenger experiments made by adding different species to the reaction mixture containing MG and T-AP_1 in order to intercept possible oxygen active species: $O_2^{\bullet-}$ (Tiron), $HO^{\bullet}$ (Tryptophan), $^1O_2$ (D-mannitol). IPA and Na_2EDTA are scavengers for the photogenerated holes, while TEMPO is a nonspecific radical trap (c). EPR measurements of selected samples in dark and under irradiation with 405 nm LED in the presence of DMPO scavenger (d); the characteristic spectral signature for DMPO/$O_2^{\bullet-}$ adduct emerges under the blue light, featuring the strongest intensity for T-AP_1. Results of the photocatalytic oxidation of Bn–OH in CH_3CN under blue LED light (e); T-CN outperforms all the P-doped CNs, which afford systematically lower conversions. Results of the photocatalytic oxidation of Bn–OH with T-CN and T-AP_1 in the presence of different amounts of HCl and TEA (f); the acid boosts the reaction in the presence of the doped catalyst, whereas the base suppresses the process.

moieties that can influence the pH of the solution and the kinetics of the overall process by their protonation/deprotonation equilibria. However, none of the specific scavengers used significantly hindered the process by trapping the target species they were meant to intercept. Therefore, the radical scavenger 2,6,6-tetramethyl-4-piperidine-*N*-oxide (TEMPO) was chosen as it is able to indistinctively and actively trap any ROS possibly generated during the photocatalytic process. The result was a much more sluggish reaction, which proved that highly reactive radicals are produced. To further investigate the chemical nature of these radicals, EPR experiments were performed in the presence of 5,5-dimethyl-1-pyrroline-*N*-oxide (DMPO) by measuring the paramagnetic signature of specific scavenger-radical adducts before and after irradiation. As shown in Figure 6d, the formation of the DMPO/$O_2^{\bullet-}$ adduct [63] was detected upon light absorption in every sample and with a higher intensity when T-AP_1 was used. This means that T-AP_1 has a higher production rate of $O_2^{\bullet-}$, which can then oxidize and mineralize the dye

23670932, 2026, 5, Downloaded from https://chemistry-europe.onlinelibrary.wiley.com/doi/10.1002/cptc.202600008 by Politecnico Di Torino Sist. Bibl Del Polit Di Torino, Wiley Online Library on [14/05/2026]. See the Terms and Conditions (https://onlinelibrary.wiley.com/terms-and-conditions) on Wiley Online Library for rules of use; OA articles are governed by the applicable Creative Commons License

molecules faster, thus following the degradation activity trend. It can be concluded that P-doped CN is active in the reduction of O_2 to $O_2^{\bullet-}$ in water via the photoexcited electrons. The produced radical species can then oxidize the dye, causing a decolorization of the solution and eventually mineralization. The acidic conditions determined by the addition of the dye can also lead to the protonation of surface-bound $O_2^{\bullet-}$ thus resulting in the production of H_2O_2 *in situ*, another active, strong oxidant species. Generally, T-AP_1 features the optimal content of phosphorus necessary to form P surface sites where photogenerated electrons can reduce O_2 rather than recombine with the holes, as is more likely to happen at higher doping percentages. This boosts the reaction rates, leading to better photocatalytic performances than T-AP_2. Furthermore, surface P sites might effectively bind molecular oxygen, fostering its reduction to hydrogen peroxide in an acidic environment. H_2O_2 colorimetric assays, indeed, revealed an improved formation of H_2O_2 that is influenced by the P content (Figure S10d in the Supporting Information). This can also be due to the more negative VB energies of P-doped CN, which may allow hydrogen peroxide production also via water oxidation. To better assess the effect of the electronic modifications induced by P-doping on catalysis, the work functions Φ of pristine and P-doped surfaces were calculated by evaluating the planar electrostatic potential (Figure S12 in the Supporting Information). The value of Φ is determined by comparing the vacuum potential to the Fermi level. Together with the positions of Kohn–Sham eigenvalues corresponding to the valence and conduction bands, it allows determining the band positions compared to the vacuum level (Figure S4 in the Supporting Information). Doping on C1 and C2 sites differed substantially in the calculated Φ (Table S3 in the Supporting Information), with a considerable jump when C1 atoms were replaced. The mixed C2/C1 was more similar to C1 in terms of Φ. The lowest energy C2 substitutions were also the ones with a trend that closely reproduces the experimental values (Figures S5 and S11 in the Supporting Information). The planar electrostatic potential analysis reveals how the work function shift $\Delta\Phi$ of the different systems is affected by the degree of P doping. A positive shift in the work function decreases the hole injection barrier, while a negative shift reduces the electron injection barrier. In the pristine T-CN, $\Delta\Phi$ is slightly positive, with a value of 20 meV. The presence of P doping has interesting effects which depend on the doping amount; at low doping (T-AP_1), $\Delta\Phi$ becomes more positive, with a value of 60 meV, indicating a further decrease in hole injection barrier and an increased yield for the oxidation of H_2O to H_2O_2. In contrast, increasing the doping amount (T-AP_2) shifts the work function to a negative value of −20 meV, suggesting that now the reduction reaction is favored.

The scope of the applicability of the T-AP series of samples was further extended by selecting three different organic substrates to test the activity of the prepared P-doped CN photocatalysts in oxidation reactions: ethylbenzene (Ph–Et), benzyl alcohol (Bn–OH), and benzyl amine (Bn–NH_2). The photocatalytic oxidation of Ph–Et is a benchmark reaction known to be driven by $O_2^{\bullet-}$ radicals [64, 65]. Nevertheless, no desired product was detected with any of the catalysts (Figure S12a in the Supporting Information). The oxidation of Bn–OH (Figure 6e) resulted in conversions from 42% to 60% with a selectivity ≥96% for the benzaldehyde product over the benzoic acid (Table S6 in the Supporting Information), while oxidative coupling of Bn–NH_2 afforded *N*-benzylbenzamide with conversions ranging from 57% to 91% (Figure S12b in the Supporting Information). In the case of Bn–OH and Bn–NH_2, T-CN outperformed the doped catalysts showing, opposite trends compared to the dye degradation. Elucidation of the reaction mechanism and the involved radical species was performed via EPR experiments with DMPO spin-trap in CH_3CN by suspending T-AP_1 and bubbling O_2, as done for the reactions in batch. The strong resonance signal arising from the formation of the DMPO/$O_2^{\bullet-}$ adduct emerged upon illumination, thus validating the photogeneration of $O_2^{\bullet-}$ by P-doped CN (Figure S12c in the Supporting Information). When the measurement was repeated, adding Bn–OH to the mixture, the intensity of the same signal under illumination was found much lower, indicating that the benzylic substrate is competing with the DMPO scavenger for $O_2^{\bullet-}$ radicals (Figure S12c in the Supporting Information). These observations are consistent with a mechanism where O_2 is first reduced to $O_2^{\bullet-}$ which then participates in the oxidation of the benzylic substrates, as already seen for the dyes photodegradation. As previously shown, the material can also produce H_2O_2 in water by photoreduction of molecular oxygen bound to the surface of the catalyst, hence colorimetric H_2O_2 assays were performed in CH_3CN following the same protocol previously used for H_2O. The results revealed a fivefold increase in H_2O_2 generation by T-AP_1 and T-AP_2 compared to the pristine CN (Figure S12d in the Supporting Information**)**. Complementary tests were also made on T-CN and T-AP_1 by adding selected quantities of HCl and triethylamine (TEA). HCl acts as a Brønsted acid by donating protons, while TEA is both a Brønsted base and an efficient hole scavenger that decreases proton availability and diverts photogenerated holes away from the substrate. Upon the addition of 0.5, 1, and 2 equivalents of HCl, a significant increase in the conversion rate was achieved, with T-AP_1 outperforming T-CN (Figure 6f), but with lower selectivity than the acid-free reaction (Table S6 in the Supporting Information). Conversely, 2 equivalents of TEA suppressed the reaction regardless of the catalyst used. In particular, the detection of benzyl benzoate in solution hints at an acid-catalyzed Fischer esterification between the produced benzoic acid and the leftover Bn–OH. Combining all the results, we ascribe the lower conversions to a stronger stabilization of $O_2^{\bullet-}$ at P-containing surface sites. This effect is competitive with the oxidation of the benzylic substrates by $O_2^{\bullet-}$, and, in the case of doped samples, there is additional competition due to H_2O_2 generation. As a result, the conversions afforded by P-doped CN are systematically lower than in the case of T-CN. The addition of acid allows the protonation of $O_2^{\bullet-}$ to H_2O_2, which then oxidizes Bn–OH to benzaldehyde, while TEA enhances the basicity of the mixture, hence resulting in an even less favored process. However, the decreasing selectivity values with increasing HCl content account for the formation of benzyl benzoate from the acid-catalyzed Fischer esterification between the produced benzoic acid and the leftover Bn–OH. Therefore, it is imperative to control the acid content in order to favor the formation of H_2O_2 without fostering parallel reactions. In general, the experiments of oxidation of benzylic substrates suggest that P-doped CN is a promising photocatalyst for H_2O_2 production via effective binding and subsequent reduction of molecular oxygen mediated by the photogenerated electrons. In particular, slightly acidic conditions favor the in situ generation of H_2O_2 and the eventual oxidation of Bn–OH, in agreement with experimental observations already reported for CN materials [49, 66–68].

23670932, 2026, 5, Downloaded from https://chemistry-europe.onlinelibrary.wiley.com/doi/10.1002/cptc.202600008 by Politecnico Di Torino Sist. Bibl Del Polit Di Torino, Wiley Online Library on [14/05/2026]. See the Terms and Conditions (https://onlinelibrary.wiley.com/terms-and-conditions) on Wiley Online Library for rules of use; OA articles are governed by the applicable Creative Commons License

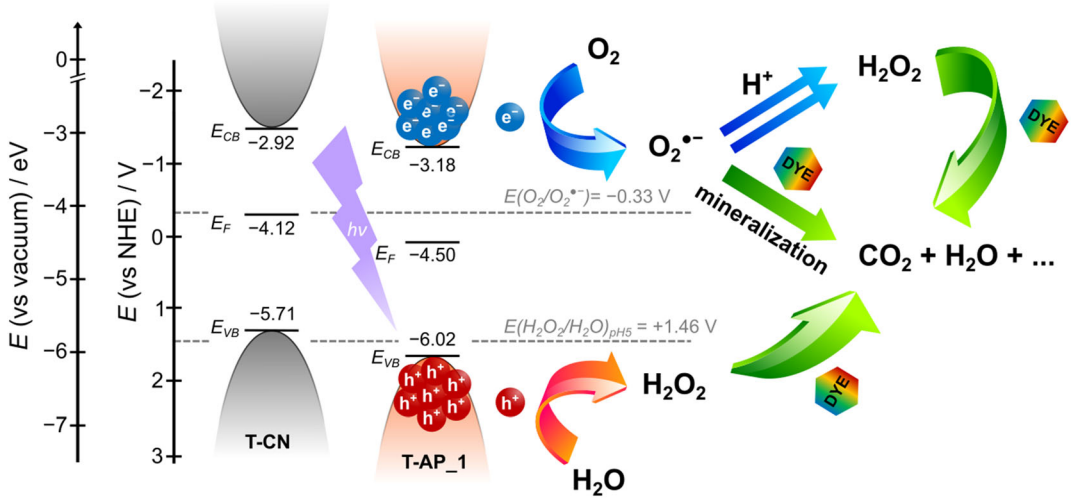

FIGURE 7 | Band diagrams of pristine T-CN (gray) and P-doped CN (orange, T-AP_1 as an example of the best performing sample) reporting the energy values of VB maximum (E_{VB}), CB minimum (E_{CB}), and Fermi level (E_F) expressed in eV units and in V on the normal hydrogen electrode scale. The two gray dashed lines refer to the potentials of the redox couples $O_2/O_2^{\bullet-}$ and H_2O_2/H_2O at pH 5 (which is determined by the addition of MG in solution). The reduction process involving the electrons is highlighted in blue: photogenerated e^- reduce O_2 to $O_2^{\bullet-}$ radical, which then is responsible for the mineralization of the dyes (green arrows) either via direct oxidation or by previous production of H_2O_2 (double blue arrow). The oxidation process involving the holes is highlighted in red: photogenerated h^+, thanks to the lower VB energies, may oxidize H_2O to H_2O_2, which can then contribute to the mineralization of the dye (green arow) The overall scheme shows that P-doped CN allows H_2O_2 formation mainly via 2-electron activation of O_2 at superficial P-sites (double blue arrow), and it shifts the VB to lower energy values that might open additional oxidative routes for H_2O_2 generation.

Eventually, the P-doped CN presented here proved to be a versatile material that can catalyze several processes under visible light and in different solvents. In water, electrons are excited to the CB upon light absorption and are used to reduce the dissolved O_2 to $O_2^{\bullet-}$, this can then generate H_2O_2 upon protonation or directly oxidize the dye molecules, leading to their mineralization and decolorization of the solution (Figure 7). The photogenerated holes may also contribute to oxidative pathways, consistent with the slightly lowered VB position in P-doped samples. Therefore, T-AP_1 has the suitable band structure to simultaneously degrade the dye and oxidize water, whereas in the pristine CN, the higher energy of the holes makes charge transfer less probable, thus leading to poor photodegradation activity. In acetonitrile, the photogenerated electrons reduce the bubbled O_2 to $O_2^{\bullet-}$, which is stabilized by the phosphorus on the surface of P-doped CN. The result is a less favorable oxidation of Bn–OH and Bn–NH_2 when T-AP_1 is used instead of T-CN, or even little to no conversion in the case of Ph–Et. Upon addition of acid, similarly to the behavior of T-AP_1 in the dye aqueous solution, $O_2^{\bullet-}$ is protonated to H_2O_2, which finally oxidizes the benzylic substrate. In this case, T-AP_1 shows improved photocatalytic performances in comparison to T-CN, as P-containing sites likely allow a better binding of O_2 to the surface of the catalyst, hence enabling the generation of a larger amount of H_2O_2. Altogether, these findings indicate that P-doped CN flexibly switches between oxidative and reductive routes depending on the reaction medium, with surface-bound oxygen intermediates playing a key mechanistic role.

3 | Conclusions

We developed a new and sustainable route to P-doped CN by simply combining thiourea and diammonium phosphate. The result is a mesoporous CN material with an improved SSA without complex processing or expensive chemicals. XPS and DFT calculations confirm that P is incorporated into the CN backbone by partial substitution of C within the heptazine framework. While the optical absorption remains generally unchanged, PL and EPR reveal that P-doping efficiently suppresses charge-carrier recombination by creating catalytically active paramagnetic centers. The improvement of the electronic properties translates into a marked enhancement of the photocatalytic performance toward the degradation of four persistent dyes, with T-AP_1 achieving the best balance between dopant density, surface area, and electronic structure. Mechanistic studies show that P-doped CN promotes O_2 activation to $O_2^{\bullet-}$ and, in mildly acidic media, to H_2O_2, enabling both the direct dye degradation and the in situ generation of additional oxidants. In organic media, the strong interactions between activated oxygen species and P sites require proton donors to drive the oxidation of benzylic substrates efficiently. Overall, this work demonstrates that phosphorus doping affords a dual-function, metal-free photocatalyst capable of flexibly operating through reductive and oxidative pathways depending on the reaction environment. The simplicity of the synthesis, coupled with improved catalytic behavior and concurrent H_2O_2 production, positions P-doped CN as a promising platform for scalable solar-driven environmental remediation and energy conversion technologies. These results provide a practical path toward the development of sustainable CN-based photocatalysts in real wastewater treatment and chemical synthesis processes.

Author Contributions

Luca Cartabia: conceptualization (equal), data curation (lead), formal analysis (lead), investigation (lead), methodology (equal), visualization (equal), writing – original draft (lead). **Yana Dubinina**: data curation (equal), formal analysis (equal), investigation (equal). **Marianna**

23670932, 2026, 5, Downloaded from https://chemistry-europe.onlinelibrary.wiley.com/doi/10.1002/cptc.202600008 by Politecnico Di Torino Sist. Bibl Del Polit Di Torino, Wiley Online Library on [14/05/2026]. See the Terms and Conditions (https://onlinelibrary.wiley.com/terms-and-conditions) on Wiley Online Library for rules of use; OA articles are governed by the applicable Creative Commons License

Barbieri: formal analysis (equal), investigation (equal), methodology (equal), writing – original draft (supporting). **Mateusz Wlazło**: data curation (equal), formal analysis (equal), investigation (equal), methodology (equal), validation (equal), writing – original draft (equal). **Pascal Schweitzer**: data curation (equal), formal analysis (equal), investigation (equal), methodology (equal), writing – original draft (supporting). **Mengjiao Wang**: formal analysis (equal), methodology (equal), project administration (supporting), supervision (supporting), validation (supporting), writing – original draft (supporting), writing – review & editing (supporting). **Francesco Lamberti**: conceptualization (supporting), formal analysis (supporting), methodology (supporting), validation (supporting), writing – review & editing (supporting). **Giorgio Zoppellaro**: data curation (supporting), formal analysis (supporting), investigation (supporting), methodology (supporting), validation (supporting), writing – original draft (supporting), writing – review & editing (supporting). **Derck Schlettwein**: formal analysis (supporting), project administration (supporting), resources (supporting), supervision (supporting), writing – review & editing (supporting). **Bernd Smarsly**: funding acquisition (supporting), resources (equal), supervision (supporting), writing – review & editing (supporting). **Silvio Osella**: formal analysis (supporting), methodology (supporting), resources (supporting), software (equal), supervision (supporting), validation (supporting), writing – original draft (supporting), writing – review & editing (supporting). **Luka Đorđević**: data curation (supporting), formal analysis (equal), funding acquisition (supporting), investigation (equal), methodology (equal), resources (equal), supervision (equal), validation (equal), writing – original draft (supporting), writing – review & editing (supporting). **Paolo Giusto**: conceptualization (equal), data curation (equal), formal analysis (equal), funding acquisition (supporting), investigation (equal), methodology (equal), project administration (equal), resources (equal), supervision (equal), validation (equal), writing – original draft (supporting), writing – review & editing (equal). **Teresa Gatti**: conceptualization (equal), funding acquisition (lead), methodology (supporting), project administration (equal), resources (equal), supervision (equal), writing – review & editing (equal).

Acknowledgments

This work was supported by the Deutsche Forschungsgemeinschaft (DFG) through project 514772236. T.G. thanks the European Research Council (ERC) for the Starting Grant project JANUS BI (grant agreement no. [101041229]). P.G. and L.C. would like to thank the Max Planck Society for financial support and Sonia Zoltowska, Bortoluya Bodomoori, and Heike Runge for help during the development of this project. P.G. would like to acknowledge the support of the funding from the European Union's Horizon Europe research and innovation program under grant agreement no. 101046836 (project acronym "CATART"). S.O. acknowledges the National Science Centre, Poland, for funding (grant no. UMO-2023/50/E/ST4/00197). L. Đ. thanks the European Research Council (ERC) for the Starting Grant project PhotoDark (grant agreement no. [101077698]). The publication reflects only the author's views and the European Union is not liable for any use that may be made of the information content therein. We gratefully acknowledge Polish high-performance computing infrastructure PLGrid (HPC Centers: ACK Cyfronet AGH) for providing computer facilities and support within computational grant no. PLG/2026/019113.

Open access publishing facilitated by Politecnico di Torino, as part of the Wiley - CRUI-CARE agreement.

Funding

This study was supported by European Research Council (101041229).

Conflicts of Interest

The authors declare no conflicts of interest.

Data Availability Statement

The data that support the findings of this study are available from the corresponding author upon reasonable request.

References

1. T. Münzel, O. Hahad, J. Lelieveld, et al., "Soil and Water Pollution and Cardiovascular Disease," *Nature Reviews Cardiology* 22 (2025): 71–89, https://doi.org/10.1038/s41569-024-01068-0.

2. M. Wang, B. L. Bodirsky, R. Rijneveld, et al., "A Triple Increase in Global River Basins with Water Scarcity due to Future Pollution," *Nature Communications* 15 (2024): 880, https://doi.org/10.1038/s41467-024-44947-3.

3. V. P. Ravinandrasana and C. L. E. Franzke, "The First Emergence of Unprecedented Global Water Scarcity in the Anthropocene," *Nature Communications* 16 (2025): 8281, https://doi.org/10.1038/s41467-025-63784-6.

4. A. Azanaw, B. Birlie, B. Teshome, and M. Jemberie, "Textile Effluent Treatment Methods and Eco-Friendly Resolution of Textile Wastewater," *Case Studies in Chemical and Environmental Engineering* 6 (2022): 100230, https://doi.org/10.1016/j.cscee.2022.100230.

5. M. M. Islam, A. R. Aidid, J. N. Mohshin, H. Mondal, S. Ganguli, and A. K. Chakraborty, "A Critical Review on Textile Dye-Containing Wastewater: Ecotoxicity, Health Risks, and Remediation Strategies for Environmental Safety," *Cleaner Chemical Engineering* 11 (2025): 100165, https://doi.org/10.1016/j.clce.2025.100165.

6. D. Cruz, S. Żółtowska, O. Savateev, M. Antonietti, and P. Giusto, "Carbon Nitride Caught in the Act of Artificial Photosynthesis," *Nature Communications* 16 (2025): 374, https://doi.org/10.1038/s41467-024-55518-x.

7. A. García-Baldoví, M. C. Antonino, L. Peng, et al., "Synergistic Effect on the Photocatalytic CO2 Hydrogenation to Methanol Using Dual Co–Cu Single Atom Poly(heptazine Imide): Influence of Pressure on Product Selectivity," *ACS Catalysis* 15 (2025): 9584–9596, https://doi.org/10.1021/acscatal.5c00827.

8. H. Liu, B. Yang, G. Liao, et al., "Facilitating Carrier Kinetics in Ultrathin Porous Carbon Nitride through Shear-Repair Strategy for Peroxymonosulfate-Assisted Water Purification," *Nature Communications* 16 (2025): 5909, https://doi.org/10.1038/s41467-025-61185-3.

9. H. Xin, Y. Liu, Y. Xiao, M. Wen, L. Sheng, and Z. Jia, "Design and Nanoengineering of Photoactive Antimicrobials for Bioapplications: From Fundamentals to Advanced Strategies," *Advanced Functional Materials* 34 (2024): 2402607, https://doi.org/10.1002/adfm.202402607.

10. J. An, H. Zhao, Z. Jia, et al., "Design and Engineering of Photocatalytic Graphitic Carbon Nitride for Environmental and Biological Disinfection," *ACS ES&T Engineering* 5 (2025): 2138–2169, https://doi.org/10.1021/acsestengg.5c00352.

11. M. Xiao, B. Luo, S. Wang, and L. Wang, "Solar Energy Conversion on g-C3N4 Photocatalyst: Light Harvesting, Charge Separation, and Surface Kinetics," *Journal of Energy Chemistry* 27 (2018): 1111–1123, https://doi.org/10.1016/j.jechem.2018.02.018.

12. D. V. Piankova, H. Zschiesche, A. P. Tyutyunnik, et al., "Enhancing the Photocatalytic Performance of Carbon Nitrides Through Controlled Local Structure Modification," *Advanced Functional Materials* 35 (2025): e11389, https://doi.org/10.1002/adfm.202511389.

13. V. W. Lau and B. V. Lotsch, "A Tour-Guide through Carbon Nitride-Land: Structure- and Dimensionality-Dependent Properties for Photo(Electro) Chemical Energy Conversion and Storage," *Advanced Energy Materials* 12 (2022): 2101078, https://doi.org/10.1002/aenm.202101078.

14. G. Algara-Siller, N. Severin, S. Y. Chong, et al., "Triazine-Based Graphitic Carbon Nitride: A Two-Dimensional Semiconductor," *Angewandte Chemie International Edition* 53 (2014): 7450–7455, https://doi.org/10.1002/anie.201402191.

23670932, 2026, 5, Downloaded from https://chemistry-europe.onlinelibrary.wiley.com/doi/10.1002/cptc.202600008 by Politecnico Di Torino Sist. Bibl Del Polit Di Torino, Wiley Online Library on [14/05/2026]. See the Terms and Conditions (https://onlinelibrary.wiley.com/terms-and-conditions) on Wiley Online Library for rules of use; OA articles are governed by the applicable Creative Commons License

15. H. Szalad, A. Galushchinskiy, T. Jianu, et al., "Polymeric Triazine/Heptazine Imide Heterostructures Enable Photocatalytic *O2 Reduction to H*2O2," *Applied Catalysis B: Environment and Energy* 357 (2024): 124323, https://doi.org/10.1016/j.apcatb.2024.124323.

16. D. Laniel, F. Trybel, A. Aslandukov, et al., "Synthesis of Ultra-Incompressible and Recoverable Carbon Nitrides Featuring CN4 Tetrahedra," *Advanced Materials* 36 (2024): 2308030, https://doi.org/10.1002/adma.202308030.

17. V. W. Lau, D. Klose, H. Kasap, et al., "Dark Photocatalysis: Storage of Solar Energy in Carbon Nitride for Time-Delayed Hydrogen Generation," *Angewandte Chemie International Edition* 56 (2017): 510–514, https://doi.org/10.1002/anie.201608553.

18. K. Eid and M. Antonietti, "Water Electrolysis Beyond Platinum: Carbon Nitride Materials for Electrochemical Hydrogen Evolution," *Advanced Science* 12 (2025): e14030, https://doi.org/10.1002/advs.202514030.

19. C. A. Caputo, L. Wang, R. Beranek, and E. Reisner, "Carbon Nitride–TiO2 Hybrid Modified with Hydrogenase for Visible Light Driven Hydrogen Production," *Chemical Science* 6 (2015): 5690–5694, https://doi.org/10.1039/C5SC02017D.

20. S. Mazzanti, B. Kurpil, B. Pieber, M. Antonietti, and A. Savateev, "Dichloromethylation of Enones by Carbon Nitride Photocatalysis," *Nature Communications* 11 (2020): 1387, https://doi.org/10.1038/s41467-020-15131-0.

21. A. Sivo, V. Ruta, V. Granata, O. Savateev, M. A. Bajada, and G. Vilé, "Nanostructured Carbon Nitride for Continuous-Flow Trifluoromethylation of (Hetero)arenes," *ACS Sustainable Chemistry & Engineering* 11 (2023): 5284–5292, https://doi.org/10.1021/acssuschemeng.3c00176.

22. J. Barrio, J. Li, and M. Shalom, "Carbon Nitrides From Supramolecular Crystals: From Single Atoms to Heterojunctions and Advanced Photoelectrodes," *Chemistry – A European Journal* 29 (2023): e202302377, https://doi.org/10.1002/chem.202302377.

23. E. Alwin, W. Nowicki, R. Wojcieszak, M. Zieliński, and M. Pietrowski, "Elucidating the Structure of the Graphitic Carbon Nitride Nanomaterials via X-Ray Photoelectron Spectroscopy and X-Ray Powder Diffraction Techniques," *Dalton Transactions* 49 (2020): 12805–12813, https://doi.org/10.1039/D0DT02325F.

24. T. S. Miller, A. d'Aleo, T. Suter, A. E. Aliev, A. Sella, and P. F. McMillan, "Pharaoh's Serpents: New Insights into a Classic Carbon Nitride Material," *Zeitschrift für Anorganische Und Allgemeine Chemie* 643 (2017): 1572–1580, https://doi.org/10.1002/zaac.201700268.

25. G. Zhang, J. Zhang, M. Zhang, and X. Wang, "Polycondensation of Thiourea into Carbon Nitride Semiconductors as Visible Light Photocatalysts," *Journal of Materials Chemistry* 22 (2012): 8083, https://doi.org/10.1039/c2jm00097k.

26. K. Maeda, X. Wang, Y. Nishihara, D. Lu, M. Antonietti, and K. Domen, "Photocatalytic Activities of Graphitic Carbon Nitride Powder for Water Reduction and Oxidation Under Visible Light," *The Journal of Physical Chemistry C* 113 (2009): 4940–4947, https://doi.org/10.1021/jp809119m.

27. A. Thomas, A. Fischer, F. Goettmann, et al., "Graphitic Carbon Nitride Materials: Variation of Structure and Morphology and Their use as Metal-Free Catalysts," *Journal of Materials Chemistry* 18 (2008): 4893, https://doi.org/10.1039/b800274f.

28. M. J. Bojdys, J.-O. Müller, M. Antonietti, and A. Thomas, "Ionothermal Synthesis of Crystalline, Condensed, Graphitic Carbon Nitride," *Chemistry – A European Journal* 14 (2008): 8177–8182, https://doi.org/10.1002/chem.200800190.

29. Y. Hong, E. Liu, J. Shi, et al., "A Direct One-Step Synthesis of Ultrathin g-C3N4 Nanosheets From Thiourea for Boosting Solar Photocatalytic H2 Evolution," *International Journal of Hydrogen Energy* 44 (2019): 7194–7204, https://doi.org/10.1016/j.ijhydene.2019.01.274.

30. W. Yang, L. Jia, P. Wu, et al., "Effect of Thermal Program on Structure–activity Relationship of g-C3N4 Prepared by Urea Pyrolysis and Its Application for Controllable Production of g-C3N4," *Journal of Solid State Chemistry* 304 (2021): 122545, https://doi.org/10.1016/j.jssc.2021.122545.

31. Y. Zhang, Q. Pan, G. Chai, et al., "Synthesis and Luminescence Mechanism of Multicolor-Emitting g-C3N4 Nanopowders by Low Temperature Thermal Condensation of Melamine," *Scientific Reports* 3 (2013): 1943, https://doi.org/10.1038/srep01943.

32. Y. Yang, J. Shi, C. Liu, et al., "Engineered Polymeric Carbon Nitride for Photocatalytic Diverse Functionalization of Electronic-Rich Alkenes," *Angewandte Chemie* 137 (2025): e202417099, https://doi.org/10.1002/ange.202417099.

33. I. F. Teixeira, N. V. Tarakina, I. F. Silva, N. López-Salas, A. Savateev, and M. Antonietti, "Overcoming Electron Transfer Efficiency Bottlenecks for Hydrogen Production in Highly Crystalline Carbon Nitride-Based Materials," *Advanced Sustainable Systems* 6 (2022): 2100429, https://doi.org/10.1002/adsu.202100429.

34. X. Tong, Y. Wu, K. Jiang, et al., "Oxygen-Doped Carbon Nitrides with Visible Room-Temperature Phosphorescence and Invisible Thermal-Stimuli-Responsive Ultraviolet Delayed Fluorescence for Security Applications," *Angewandte Chemie* 137 (2025): e202415312, https://doi.org/10.1002/ange.202415312.

35. B. Abed, V. R. Battula, M. Volokh, et al., "Selective Toluene Oxidation Using Sulfur-Doped Polymeric Carbon Nitride Photocatalysts," *Small* 21 (2025): 2501230, https://doi.org/10.1002/smll.202501230.

36. P. Giusto, H. Arazoe, D. Cruz, et al., "Boron Carbon Nitride Thin Films: From Disordered to Ordered Conjugated Ternary Materials," *Journal of the American Chemical Society* 142 (2020): 20883–20891, https://doi.org/10.1021/jacs.0c10945.

37. T. Ji, Y. Guo, H. Liu, B. Chang, X. Wei, and B. Yang, "Growth of Narrow-Bandgap Cl-Doped Carbon Nitride Nanofibers on Carbon Nitride Nanosheets for High-Efficiency Photocatalytic H2O2 Generation," *RSC Advances* 11 (2021): 31385–31394, https://doi.org/10.1039/D1RA05787A.

38. G. Zhang, M. Zhang, X. Ye, X. Qiu, S. Lin, and X. Wang, "Iodine Modified Carbon Nitride Semiconductors as Visible Light Photocatalysts for Hydrogen Evolution," *Advanced Materials* 26 (2014): 805–809, https://doi.org/10.1002/adma.201303611.

39. Z.-A. Lan, G. Zhang, and X. Wang, "A Facile Synthesis of Br-Modified g-C3N4 Semiconductors for Photoredox Water Splitting," *Applied Catalysis B: Environmental* 192 (2016): 116–125, https://doi.org/10.1016/j.apcatb.2016.03.062.

40. S. Zhao, Y. Liu, Y. Wang, et al., "Carbon and Phosphorus Co-Doped Carbon Nitride Hollow Tube for Improved Photocatalytic Hydrogen Evolution," *Journal of Colloid and Interface Science* 616 (2022): 152–162, https://doi.org/10.1016/j.jcis.2022.02.057.

41. W. Gao, G. Li, Y. Shao, et al., "Interfacial Phosphorus Doping into in-Plane Carbon Rings/Carbon Nitride for Enhancing High-Value H_2O_2 Photosynthesis," *Chemical Engineering Journal* 521 (2025): 166614, https://doi.org/10.1016/j.cej.2025.166614.

42. Z. Zhao, Y. Long, Y. Chen, F. Zhang, and J. Ma, "Phosphorus Doped Carbon Nitride with Rich Nitrogen Vacancy to Enhance the Electrocatalytic Activity for Nitrogen Reduction Reaction," *Chemical Engineering Journal* 430 (2022): 132682, https://doi.org/10.1016/j.cej.2021.132682.

43. Y.-Z. Huang, Y.-S. Lin, Y.-S. Lin, T.-C. Chiu, and C.-C. Hu, "Phosphorus-Doped Carbon Nitride Materials for Enhanced Photocatalytic Degradation of Organic Pollutants Under Visible-Light Irradiation," *ACS Omega* 10 (2025): 41457–41466, https://doi.org/10.1021/acsomega.5c04783.

44. K. Abbas, M. Javed, S. Aslam, et al., "Co-Application of Potassium and Thiourea for Mitigating Salinity Stress in Wheat Seedlings," *Scientific Reports* 15 (2025): 14689, https://doi.org/10.1038/s41598-025-98878-0.

23670932, 2026, 5, Downloaded from https://chemistry-europe.onlinelibrary.wiley.com/doi/10.1002/cptc.202600008 by Politecnico Di Torino Sist. Bibl Del Polit Di Torino, Wiley Online Library on [14/05/2026]. See the Terms and Conditions (https://onlinelibrary.wiley.com/terms-and-conditions) on Wiley Online Library for rules of use; OA articles are governed by the applicable Creative Commons License

45. L. DuPlooy, J. Heitman, L. Gatiboni, and A. Amoozegar, "Transport of Phosphorus From Three Fertilizers Through High- and Low-Phosphorus Soils," *Agronomy* 15 (2025): 2395, https://doi.org/10.3390/agronomy15102395.

46. M. Thommes, K. Kaneko, A. V. Neimark, et al., "Physisorption of Gases, with Special Reference to the Evaluation of Surface Area and Pore Size Distribution (IUPAC Technical Report)," *Pure and Applied Chemistry* 87 (2015): 1051–1069, https://doi.org/10.1515/pac-2014-1117.

47. C. Schlumberger and M. Thommes, "Characterization of Hierarchically Ordered Porous Materials by Physisorption and Mercury Porosimetry—A Tutorial Review," *Advanced Materials Interfaces* 8 (2021): 2002181, https://doi.org/10.1002/admi.202002181.

48. B. Sun, H. Yu, Y. Yang, et al., "New Complete Assignment of X-Ray Powder Diffraction Patterns in Graphitic Carbon Nitride Using Discrete Fourier Transform and Direct Experimental Evidence," *Physical Chemistry Chemical Physics* 19 (2017): 26072–26084, https://doi.org/10.1039/C7CP05242A.

49. B. Long, Z. Ding, and X. Wang, "Carbon Nitride for the Selective Oxidation of Aromatic Alcohols in Water Under Visible Light," *ChemSusChem* 6 (2013): 2074–2078, https://doi.org/10.1002/cssc.201300360.

50. F. Dong, Z. Wang, Y. Sun, W.-K. Ho, and H. Zhang, "Engineering the Nanoarchitecture and Texture of Polymeric Carbon Nitride Semiconductor for Enhanced Visible Light Photocatalytic Activity," *Journal of Colloid and Interface Science* 401 (2013): 70–79, https://doi.org/10.1016/j.jcis.2013.03.034.

51. R. Škuta, V. Matějka, K. Foniok, et al., "On P-Doping of Graphitic Carbon Nitride with Hexachlorotriphosphazene as a Source of Phosphorus," *Applied Surface Science* 552 (2021): 149490, https://doi.org/10.1016/j.apsusc.2021.149490.

52. P. Giusto, B. Kumru, J. Zhang, R. Rothe, and M. Antonietti, "Let a Hundred Polymers Bloom: Tunable Wetting of Photografted Polymer-Carbon Nitride Surfaces," *Chemistry of Materials* 32 (2020): 7284–7291, https://doi.org/10.1021/acs.chemmater.0c01798.

53. A. B. Boscoletto, M. Gleria, R. Milani, L. Meda, and R. Bertani, "Surface Functionalization with Phosphazene Substrates—part VII. Silicon-Based Materials Functionalized with Hexachlorocyclophosphazene," *Surface and Interface Analysis* 41 (2009): 27–33, https://doi.org/10.1002/sia.2967.

54. J. Liu, H. Liu, Y. Zhang, et al., "Synthesis and Characterization of Phosphorus–nitrogen Doped Multiwalled Carbon Nanotubes," *Carbon* 49 (2011): 5014–5021, https://doi.org/10.1016/j.carbon.2011.07.018.

55. M. A. Quintana, A. Picón, M. Á. Martín-Lara, M. Calero, M. J. Muñoz-Batista, and R. R. Solís, "Towards the Photocatalytic Production of Cinnamaldehyde with Phosphorous-Tailored Graphitic-Like Carbon Nitride," *Applied Catalysis A: General* 674 (2024): 119607, https://doi.org/10.1016/j.apcata.2024.119607.

56. S. Bhowmik, T. Pal, D. D. Khubchandani, and P. K. Iyer, "Understanding the Structural Intricacies in Carbon Nitride Materials through Multimodal Characterization: A Critical Review," *Journal of Physics: Condensed Matter* 37 (2025): 463003, https://doi.org/10.1088/1361-648X/ae191f.

57. P. Makuła, M. Pacia, and W. Macyk, "How To Correctly Determine the Band Gap Energy of Modified Semiconductor Photocatalysts Based on UV–Vis Spectra," *The Journal of Physical Chemistry Letters* 9 (2018): 6814–6817, https://doi.org/10.1021/acs.jpclett.8b02892.

58. R. Godin and J. R. Durrant, "Dynamics of Photoconversion Processes: The Energetic Cost of Lifetime Gain in Photosynthetic and Photovoltaic Systems," *Chemical Society Reviews* 50 (2021): 13372–13409, https://doi.org/10.1039/D1CS00577D.

59. A. Actis, P. Fornasiero, M. Chiesa, and E. Salvadori, "Photo-Induced Radicals in Carbon Nitride and Their Magnetic Signature," *ChemPhotoChem* 8 (2024): e202300203, https://doi.org/10.1002/cptc.202300203.

60. A. Ma, H. Qian, H. Liu, and S. Ren, "Degradation of Malachite Green by g-C3N4-Modified Magnetic Attapulgite Composites Under Visible-Light Conditions," *Environmental Science and Pollution Research* 30 (2023): 96360–96375, https://doi.org/10.1007/s11356-023-29201-5.

61. K. Mhalshekar, S. Selvam, A. Sahoo, M. P. Illa, M. Gaydhane, and S. Sontakke, "Efficient Photocatalytic Degradation of Malachite Green and Cr(VI) Using Co-MOF and Bacterial Cellulose@Co-MOF Biocomposite: A Green Approach," *ACS Omega* 10 (2025): 45965–45981, https://doi.org/10.1021/acsomega.5c06750.

62. P. A. Ajibade and T. B. Mbuyazi, "Photocatalytic Degradation of Single and Binary Mixture of Malachite Green and Rhodamine B Dyes by Biochar-Capped Iron Oxide Nanocomposites," *Environmental Science and Pollution Research* 32 (2025): 23588–23606, https://doi.org/10.1007/s11356-025-37025-8.

63. K. Makino, T. Hagiwara, and A. Murakami, "A Mini Review: Fundamental Aspects of Spin Trapping with DMPO," *International Journal of Radiation Applications and Instrumentation. Part C. Radiation Physics and Chemistry* 37 (1991): 657–665, https://doi.org/10.1016/1359-0197(91)90164-W.

64. M. Xia, H. Huang, X. Zhang, Q.-H. Wei, and Z. Xie, "Single-Atom Cobalt-Fused Biomolecule-Derived Nitrogen-Doped Carbon Nanosheets for Selective Oxidation Reactions," *Physical Chemistry Chemical Physics* 23 (2021): 14276–14283, https://doi.org/10.1039/D1CP01113H.

65. H. Zhu, J. Zhao, C. Ma, Z. Yu, J. Li, and Q. Meng, "Bridging Effect of Carbon Nitride with More Negative Conduction Potential and Halogens Promotes the Liquid-Phase Oxidation of Aromatic C–H Bonds," *ACS Applied Materials & Interfaces* 15 (2023): 59280–59295, https://doi.org/10.1021/acsami.3c08461.

66. O. Savateev, "Selective Oxidation of Alcohols Using Carbon Nitride Photocatalysts," in *UV-Visible Photocatalysis for Clean Energy Production and Pollution Remediation*, (John Wiley & Sons, Ltd., 2023), ISBN: 978-3–527–83799–1.

67. F. Su, S. C. Mathew, L. Möhlmann, M. Antonietti, X. Wang, and S. Blechert, "Aerobic Oxidative Coupling of Amines by Carbon Nitride Photocatalysis with Visible Light," *Angewandte Chemie International Edition* 50 (2011): 657–660, https://doi.org/10.1002/anie.201004365.

68. F. Su, S. C. Mathew, G. Lipner, et al., "Mpg-C_3N_4 -Catalyzed Selective Oxidation of Alcohols Using O_2 and Visible Light," *Journal of the American Chemical Society* 132 (2010): 16299–16301, https://doi.org/10.1021/ja102866p.

69. P. D. Josephy, T. Eling, and R. P. Mason, "The Horseradish Peroxidase-Catalyzed Oxidation of 3,5,3′,5′-Tetramethylbenzidine. Free Radical and Charge-Transfer Complex Intermediates," *Journal of Biological Chemistry* 257 (1982): 3669–3675, https://doi.org/10.1016/S0021-9258(18)34832-4.

70. M. Jakešová, D. H. Apaydin, M. Sytnyk, et al., "Hydrogen-Bonded Organic Semiconductors as Stable Photoelectrocatalysts for Efficient Hydrogen Peroxide Photosynthesis," *Advanced Functional Materials* 26 (2016): 5248–5254, https://doi.org/10.1002/adfm.201601946.

71. F. Arcudi, L. Đorđević, N. Schweitzer, S. I. Stupp, and E. A. Weiss, "Selective Visible-Light Photocatalysis of Acetylene to Ethylene Using a Cobalt Molecular Catalyst and Water as a Proton Source," *Nature Chemistry* 14 (2022): 1007–1012, https://doi.org/10.1038/s41557-022-00966-5.

72. P. A. F. Garrillo, B. Grévin, N. Chevalier, and Ł. Borowik, "Calibrated Work Function Mapping by Kelvin Probe Force Microscopy," *Review of Scientific Instruments* 89 (2018): 043702, https://doi.org/10.1063/1.5007619.

Supporting Information

Additional supporting information can be found online in the Supporting Information section. The authors have cited additional references within the Supporting Information [69–72].

23670932, 2026, 5, Downloaded from https://chemistry-europe.onlinelibrary.wiley.com/doi/10.1002/cptc.202600008 by Politecnico Di Torino Sist. Bibl Del Polit Di Torino, Wiley Online Library on [14/05/2026]. See the Terms and Conditions (https://onlinelibrary.wiley.com/terms-and-conditions) on Wiley Online Library for rules of use; OA articles are governed by the applicable Creative Commons License